

P-Mamba: Marrying Perona Malik Diffusion with Mamba for Efficient Pediatric Echocardiographic Left Ventricular Segmentation

Zi Ye^{1,2}, Tianxiang Chen³, Fangyijie Wang⁴, Hanwei Zhang^{1,5}, Guanxi Li⁶, and Lijun Zhang^{1,7}

¹ Institute of Intelligent Software, Guangzhou, China

² RuiJin Hospital LuWan Branch, Shanghai Jiaotong University School of Medicine, Shanghai, China
yezi1022@gmail.com

³ University of Science and Technology of China, China
txchen@mail.ustc.edu.cn

⁴ School of Medicine, University College Dublin, Dublin, Ireland
fangyijie.wang@ucdconnect.ie

⁵ Saarland University, Germany
zhang@depend.uni-saarland.de

⁶ South China University of Technology, Guangzhou, China
liguanxi0809@163.com

⁷ SKLCS, Institute of Software, University of Chinese Academy of Sciences
zhanglj@ios.ac.cn

Abstract. In pediatric cardiology, the accurate and immediate assessment of cardiac function through echocardiography is important since it can determine whether urgent intervention is required in many emergencies. However, echocardiography is characterized by ambiguity and heavy background noise interference, bringing more difficulty to accurate segmentation. Present methods lack efficiency and are also prone to mistakenly segmenting some background noise areas as the left ventricular area due to noise disturbance. To relieve the two issues, we introduce P-Mamba for efficient pediatric echocardiographic left ventricular segmentation. Specifically, we turn to the recently proposed vision mamba layers in our vision mamba encoder branch to improve the computing and memory efficiency of our model while modeling global dependencies. In the other DWT-based PMD encoder branch, we devise DWT-based Perona-Malik Diffusion (PMD) Blocks that utilize PMD for noise suppression, while simultaneously preserving the local shape cues of the left ventricle. Leveraging the strengths of both the two encoder branches, P-Mamba achieves superior accuracy and efficiency to established models, such as vision transformers with quadratic and linear computational complexity. This innovative approach promises significant advancements in pediatric cardiac imaging and beyond.

Keywords: Pediatric Echocardiographic Left Ventricular Segmentation · Mamba · Perona–Malik Diffusion.

1 Introduction

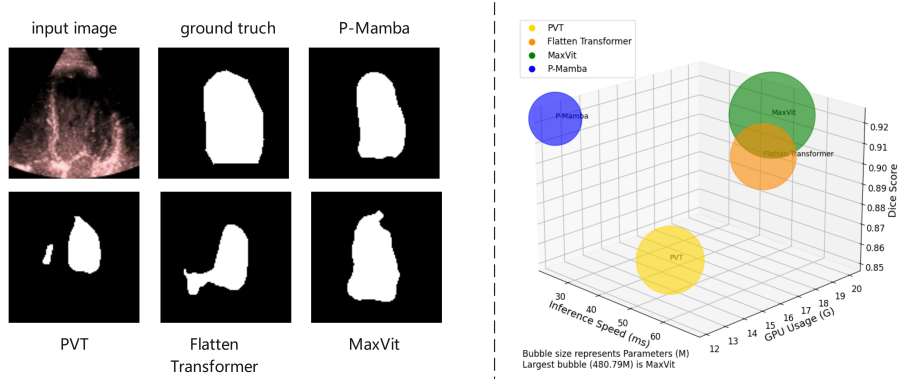


Fig. 1. (left) Visualization of the noise interference challenge and (right) efficiency comparisons between P-Mamba and other models on the PSAX dataset.

Congenital heart diseases (CHD) pose significant health risks, necessitating precise diagnostic tools like the Echocardiogram for early detection and treatment in children. Accurate segmentation of cardiac structures in pediatric echocardiographic images is crucial, particularly for calculating the Left Ventricular Ejection Fraction (LVEF), a vital metric for assessing systolic function using the biplane Simpson’s method [1]. However, challenges remain due to the background noise interference in echocardiography, leading to some inaccuracies in the shape-aware segmentation of the left ventricle. Also, segmentation efficiency is another concern. Thus, the need for precision and efficiency in this essential diagnostic procedure should be emphasized [2].

Recent studies show that artificial intelligence (AI) has improved the accuracy of assessing left ventricular (LV) function in adult echocardiography. However, applying these technologies to pediatric echocardiography is challenging due to the variability in anatomical abnormalities, heart rate, size, and patient cooperation, which affect image quality [3]. Despite these obstacles, AI has made strides in pediatric cardiology. Innovative algorithms like the Dual Attention Enhancement Feature Fusion Network [4], the Attention-Guided Dual-Path Network (AIDAN) [5], alongside the Multi-Scale Wavelet Network (MS-Net) that employs wavelet transforms for noise reduction [6].

Nevertheless, current approaches easily mistake some background noise areas for the target area and also are not efficient enough, as shown in Fig. 1. To address the challenges, we proposed an innovative architecture for pediatric echocardiographic LV segmentation named P-Mamba. This model can eliminate noise while preserving the local target boundary details to achieve the best performance. At the same time, our model demonstrates superior efficiency.

Our P-Mamba draws inspiration from the selective structured state space model Mamba [7] and Perona–Malik Diffusion (PMD) [9]. Mamba is a contemporary state space model that can better capture long-range dependencies than transformers. It is also a hardware-aware model with linear complexity to guarantee the high efficiency of the training and inference processes. On the other hand, PMD is an image-processing technique that reduces noise without preserving edge details.

Our main contributions are as follows:

- We propose P-Mamba, which innovatively combines the PMD branch’s noise suppression and local feature extraction ability with the vision Mamba’s efficient design for global dependency modeling, to set new performance benchmarks on noisy pediatric echocardiogram datasets.
- Benefiting from PMD, our model excels by suppressing noise while preserving and enhancing target edges in ultrasound images.
- Extensive experiments demonstrate that our P-Mamba achieves superior segmentation accuracy and efficiency to other methods, including vision transformers with quadratic [13] and linear [14,15] computational complexity.

2 Methodology

As shown in Fig. 2 (left), the P-Mamba is divided into three components: the Vision Mamba encoder branch, the DWT-based PMD encoder branch, and the decoders. Four feature maps are produced as outputs of the Vision Mamba branch, each at descending resolutions of 1/4, 1/8, 1/16, and 1/32 relative to the original input size while progressively increasing the channels at each level. Similarly, the DWT-based PMD branch generates four feature outputs with resolutions and channel dimensions identical to those of the Vision Mamba branch. The Vision Mamba branch is designed to guarantee the high efficiency of our model while encapsulating global dependencies. The DWT-based PMD branch complements with the mamba branch, suppressing background noise interference while preserving target edges to capture more local target features.

In the decoding stage, the output feature maps from both the Vision Mamba and DWT-based PMD branches are combined and then passed through the Segmentation Head (SegHead) decoder and the Fully Convolutional Network Head (FCNHead) decoder. These decoders intake four-scale input features and up-sample the features to produce segmentation masks. Each decoder is supervised by a loss function to enhance the overall network performance.

2.1 DWT-based PMD Block

Originally used in image de-noising tasks, Perona-Malik Diffusion (PMD) can suppress noise disturbance while preserving boundary details. Considering that echocardiograms contain heavy background noise that may interfere with segmentation accuracy, we propose the DWT-based PMD Block (shown in Fig. 3)

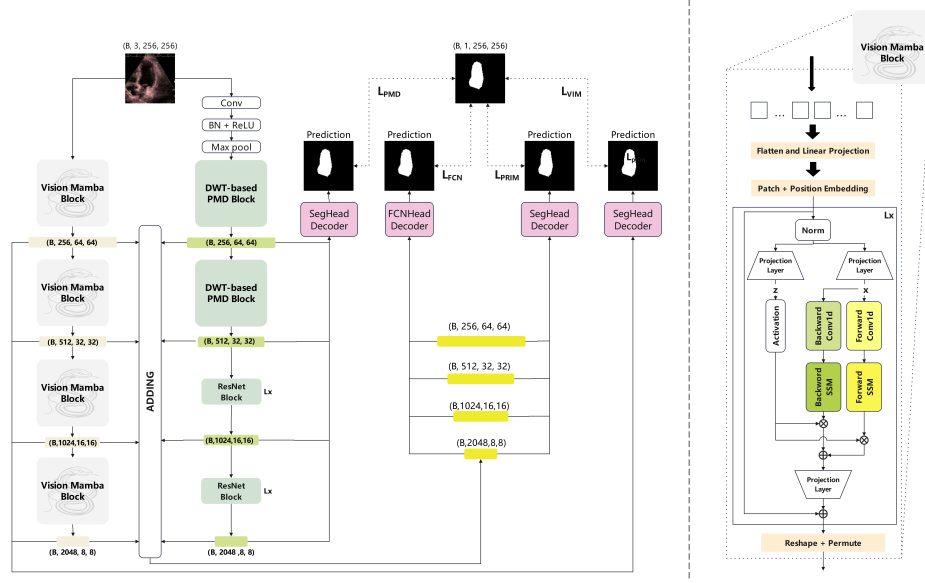


Fig. 2. The structure of our P-Mamba (left) and the Vision Mamba block (right).

to act on feature maps so that the background noise can be filtered while some target boundary cues can be preserved.

Given an input feature map u , its PMD equation can be expressed as:

$$\frac{\partial u}{\partial t} = \text{div} (g(|\nabla u|) \nabla u) \quad (1)$$

where $g(|\nabla u|) = \frac{1}{1 + (\frac{|\nabla u|}{k})^2}$ is the diffusion coefficient; t is the diffusion step and can be regarded as the layer of the feature map; k is a positive constant to control the degree of diffusion and is set to 1 by default in our experiments. Notably, Equation (1) is an anisotropic diffusion equation: in the flat or smooth regions where the gradient magnitude is small ($|\nabla u| \rightarrow 0$), the diffusion coefficient g is large, meaning that the diffusion is strong and Equation (1) acts as Gaussian smoothing to remove the noise interference. Somewhere near the target's boundary, the gradient magnitude is large ($|\nabla u| \rightarrow 1$), so the coefficient g is near zero, meaning the diffusion is weak, and the boundary details can be preserved. Equation (1) can also be rewritten to the following form:

$$\begin{aligned} \frac{\partial u}{\partial t} = & \frac{\partial}{\partial x} \left\{ g \left(\sqrt{\left(\frac{\partial u_k}{\partial x} \right)^2 + \left(\frac{\partial u_k}{\partial y} \right)^2} \right) \frac{\partial u_k}{\partial x} \right\} \\ & + \frac{\partial}{\partial y} \left\{ g \left(\sqrt{\left(\frac{\partial u_k}{\partial x} \right)^2 + \left(\frac{\partial u_k}{\partial y} \right)^2} \right) \frac{\partial u_k}{\partial y} \right\} \end{aligned} \quad (2)$$

where $\frac{\partial u}{\partial x}$ and $\frac{\partial u}{\partial y}$ represent the gradients of the feature map in horizontal and vertical directions. On the other hand, the Discrete Wavelet Transform (DWT) of an input feature map can be expressed as:

$$u_i = DWT(u), i \in \{u_{LL}, u_{LH}, u_{HL}, u_{HH}\} \quad (3)$$

where u_{LL} is the low-frequency part of the feature map, while u_{LH} , u_{HL} and u_{HH} are the high-frequency parts in horizontal, vertical and diagonal directions of the feature map which mainly contain the boundary details. By approximating the derivative terms $\frac{\partial u}{\partial x}$ with u_{LH} and $\frac{\partial u}{\partial y}$ with u_{HL} and setting the diffusion step size δt to one, we can transform Equation (2) to the discrete format:

$$u_k = u_{k-1} + \left[g \left(\sqrt{u_{LH}^2 + u_{HL}^2} \right) \cdot u_{LH} \right]_{LH} + \left[g \left(\sqrt{u_{LH}^2 + u_{HL}^2} \right) \cdot u_{HL} \right]_{HL} \quad (4)$$

After enhancing the feature map by PMD, we feed the diffusion output into a basic ResNet block. By piling multiple DWT-based PMD blocks in all layers of one encoder branch, our P-Mamba is equipped with the ability to suppress background noise disturbance while preserving the target boundary features.

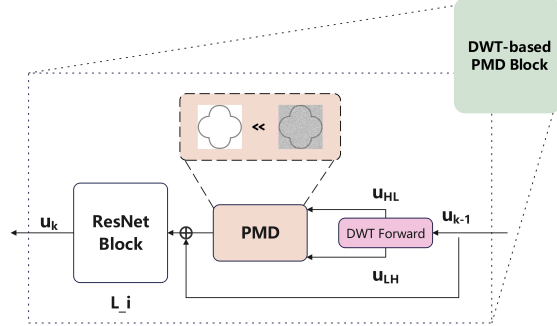


Fig. 3. Structure of DWT-based PMD Block. Layer number $L_i \in \{3, 4, 6, 3\}, i = 1, 2, 3, 4$.

2.2 Vision Mamba Block

An overview of the Vision Mamba Block, deriving from Vim [17], is depicted in Fig. 2 (right). We adopt the vision mamba layer here mainly to improve our model’s computing and memory efficiency. Also, It helps capture global dependencies complementary to the local shape cues extracted by our DWT-based PMD encoder branch.

In the initial stage, a 2-D input $\in \mathbb{R}^{H \times W \times C}$ is transformed into flattened patches P_N with dimensions $M \times (N^2 \cdot C)$. Here (H, W) is the size of the original

input, C stands for the number of channels, and N and M denote the size and total count of segmented patches, respectively. Then, the P_N is linearly projected to vectors of dimension D and add position embedding $E_{\text{pos}} \in \mathbb{R}^{M \times D}$. This process can be described as follows:

$$X_0 = [x^1W; x^2W; \dots; x^MW] + E_{\text{pos}} \quad (5)$$

where X^M is the M^{th} patch of P_N , $W \in \mathbb{R}^{(N^2 \cdot C) \times D}$ is the learnable projection matrix. The token sequence from the previous layer, X_{l-1} , is processed by the l^{th} layer vision mamba encoder to obtain the output X_l , which is expressed by Equation (6). Subsequently, X_l is reshaped and permuted to be the next stage’s input, and then repeat the above operations to get the next stage output.

$$X_l = \text{Vim}(X_{l-1}) + X_{l-1} \quad (6)$$

2.3 Loss Function

The paper uses cross-entropy loss functions exclusively, comprising a primary loss function $\mathcal{L}_{\text{prim}}$ and three auxiliary loss functions \mathcal{L}_{fcn} , \mathcal{L}_{pmd} , \mathcal{L}_{vim} , i.e., $\mathcal{L}_{\text{prim}}$ for the fusion brand with SegHead, \mathcal{L}_{fcn} for fusion brand with FCNHead, \mathcal{L}_{pmd} for DWT-based PMD Blcok brand, \mathcal{L}_{vim} for Vision Mamba Block brand.

3 Experiment Results and Analysis

3.1 Datasets

This study utilized a dataset of 4,467 echocardiograms from 1,958 pediatric patients, collected from Lucile Packard Children’s Hospital Stanford (2014-2021), divided into training (80%), testing (10%), and validation (10%) sets [18]. The dataset included 7,643 grayscale 2D video clips and 17,600 labeled images.

3.2 Implementation Details and Evaluation Metrics

The experiments were conducted using a hardware setup consisting of a Tesla V100-32GB GPU, a 12-core CPU, and 61GB of RAM, all running on an Ubuntu 18 system with CUDA 11.0 and PyTorch version 1.13. Throughout the experiments, a total of 300 epochs were conducted with a learning rate set at 0.0001 and a batch size of 16, incorporating an input size of 256×256 . The architecture included a DWT-based PMD branch with 3, 4, 6, and 3 blocks per stage and a Vision Mamba branch with two blocks per stage. Precision, Recall, and Dice coefficients are used as metrics to evaluate these methods on both datasets.

Table 1. Comparison with the state-of-the-art methods.

Methods	PSAX Dataset			A4C Dataset		
	Precision	Recall	Dice	Precision	Recall	Dice
UNet (FCN) [10]	0.8492	0.8761	0.8624	0.8279	0.8345	0.8312
UNet (PSPNet) [10]	0.8517	0.8854	0.8682	0.8076	0.8612	0.8336
ResNet-50 [16]	0.89	0.909	0.8994	0.8837	0.8773	0.8805
PVT [13]	0.867	0.8366	0.8515	0.7166	0.6553	0.6846
UniFormer [11]	0.9100	0.9134	0.9073	0.8969	0.8915	0.8918
SpectFormer [12]	0.9127	0.9063	0.9161	0.9076	0.9035	0.9010
Flatten Transformer [14]	0.9215	0.9122	0.9168	0.913	0.8832	0.8978
MaxVit [15]	0.9024	0.9249	0.9135	0.8912	0.9066	0.8988
Ours	0.9316	0.9128	0.9221	0.9025	0.9067	0.9046

3.3 Result Comparisons

In Table 1 we offer the quantitative comparison of our P-Mamba with some CNN-based methods like U-Net with FCN [10] and PSPNet [10] backbones, ResNet50 [16], and ViT-based SOTA approaches such as PVT [13], Flatten Transformer [14], and MaxVit [15]. Results show the superiority of P-Mamba on the pediatric LV 2D segmentation task, achieving the best average DSC of 0.9221 and 0.9056 on PSAX and A4C datasets, respectively. We also provide the visual comparison results in Fig. 4 (a), where our P-Mamba is the least affected by noise interference and enjoys the best segmentation effect, thanks to our PMD design. Fig. 4 (b) visualizes the intermediate feature maps of the PMD encoder branch to display the gradual noise suppression and shape detail preservation process.

Table 2. Ablation study on the DWT-based PMD Block design.

Methods	PSAX Dataset			A4C Dataset		
	Precision	Recall	Dice	Precision	Recall	Dice
Ours w/o PMD	0.9199	0.9187	0.9193	0.9132	0.8867	0.8997
Ours w/ Sobel	0.9312	0.9013	0.9160	0.9073	0.8983	0.9028
Ours	0.9316	0.9128	0.9221	0.9025	0.9067	0.9046

3.4 Ablation Studies

We first ablate the DWT-based PMD Block in Table 2 across various configurations: 'Ours w/o PMD,' means removing the DWT-based PMD part; 'Ours w/ Sobel' means replacing the DWT-based PMD part with a Sobel operator, which is only for edge preservation. Our DWT-based PMD block achieves the best performance on both datasets. The DWT-based PMD part encompasses

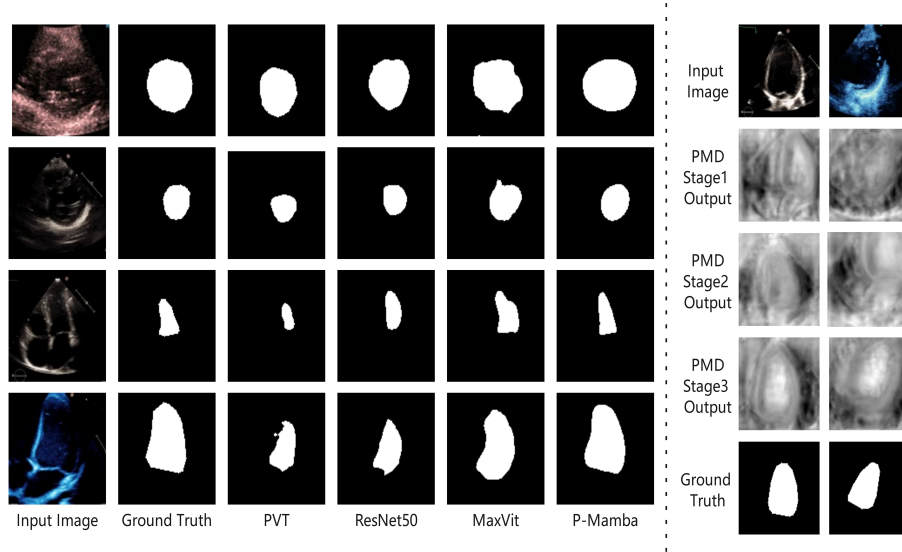


Fig. 4. The visual comparison of different methods

Table 3. Ablation study on the Vision Mamba Block design.

Methods	PSAX Dataset			A4C Dataset		
	Precision	Recall	Dice	Precision	Recall	Dice
Mamba → PVT	0.9029	0.9183	0.9105	0.9045	0.8714	0.8876
Mamba → Flatten Transformer	0.9137	0.9157	0.9147	0.9228	0.8752	0.8984
Mamba → MaxVit	0.9253	0.9087	0.9169	0.9062	0.9013	0.9038
Ours	0.9316	0.9128	0.9221	0.9025	0.9067	0.9046

the Sobel operator due to its capability of noise suppression and edge preservation, while the Sobel operator cannot curtail noise interference.

Table 3 studies the effect of the vision Mamba block, we replaced the Mamba branch with ViT structures with quadratic (PVT) and linear complexity (Flatten ViT, MaxViT), respectively. Our findings indicate that Vision Mamba can be more accurate than other models with linear or quadratic complexity.

3.5 Model Efficiency Comparison

Table 4 presents the model efficiency comparison results of P-Mamba with some SOTA ViT methods with quadratic and linear complexity in terms of parameters, inference speed (ms), GPU memory usage, and GFLOPs, where our P-Mamba significantly outperforms other methods in all metrics. The attention-free design of our Mamba branch significantly improves model efficiency even compared with linear complexity models. Our DWT-based PMD block brings no excessive parameters compared with the light ResNet block. Thus, our model is very efficient.

Table 4. Model efficiency comparison regarding parameter number (M), inference speed (ms), GPU memory (GB), and GFLOPs.

Methods	#Params	Inference Speed	GPU memory	GFLOPs
PVT [13]	299.81	40.39	15.39	181.88
Flatten Transformer [14]	282.57	67.48	15.55	144.45
MaxVit [15]	480.79	46.29	20.08	259.48
Ours	183.37	23.49	12.22	71.81

4 Conclusion

To address the challenges of noise interference and model inefficiency, we propose P-Mamba for pediatric echocardiographic left ventricular segmentation. P-Mamba uses vision mamba layers to improve computing and memory efficiency while capturing global dependencies. Additionally, it incorporates DWT-based Perona-Malik Diffusion Blocks to suppress noise and maintain local ventricular shape details. P-Mamba outperforms existing models, offering both higher accuracy and efficiency in pediatric cardiac imaging.

References

1. Van Der Linde, D., Konings, E. E., Slager, M. A., Witsenburg, M., Helbing, W. A., Takkenberg, J. J., & Roos-Hesselink, J. W. (2011). Birth prevalence of congenital heart disease worldwide: a systematic review and meta-analysis. *Journal of the American College of Cardiology*, **58**(21), 2241–2247. <https://doi.org/10.1016/j.jacc.2011.08.025>

2. Xu, L., Liu, M., Zhang, J., & He, Y. (2020). Convolutional-neural-network-based approach for segmentation of apical four-chamber view from fetal echocardiography. *IEEE Access*, **8**, 80437–80446.
3. Power, A., Poonja, S., Disler, D., Myers, K., Patton, D. J., Mah, J. K., Fine, N. M., & Greenway, S. C. (2017). Echocardiographic image quality deteriorates with age in children and young adults with Duchenne muscular dystrophy. *Frontiers in cardiovascular medicine*, **4**, 82. <https://doi.org/10.3389/fcvm.2017.00082>
4. Guo, L., Lei, B., Chen, W., Du, J., Frangi, A. F., Qin, J., Zhao, C., Shi, P., Xia, B., & Wang, T. (2021). Dual attention enhancement feature fusion network for segmentation and quantitative analysis of pediatric echocardiography. *Medical Image Analysis*, **71**, 102042. <https://doi.org/10.1016/j.media.2021.102042>
5. Hu, Y., Xia, B., Mao, M., Jin, Z., Du, J., Guo, L., Frangi, A. F., Lei, B., & Wang, T. (2020). AIDAN: an attention-guided dual-path network for pediatric echocardiography segmentation. *IEEE Access*, **8**, 29176–29187. <https://doi.org/10.1109/ACCESS.2020.2971383>
6. Zhao, C., Xia, B., Chen, W., Guo, L., Du, J., Wang, T., & Lei, B. (2021). Multi-scale wavelet network algorithm for pediatric echocardiographic segmentation via hierarchical feature guided fusion. *Applied Soft Computing*, **107**, 107386. <https://doi.org/10.1016/j.asoc.2021.107386>
7. Gu, A., & Dao, T. (2023). Mamba: Linear-time sequence modeling with selective state spaces. *arXiv preprint arXiv:2312.00752*. <https://doi.org/10.48550/arXiv.2312.00752>
8. Cotter, F. (2019). Uses of Complex Wavelets in Deep Convolutional Neural Networks. Apollo - University of Cambridge Repository. <https://www.repository.cam.ac.uk/handle/1810/306661>. <https://doi.org/10.17863/CAM.53748>
9. Perona, P., & Malik, J. (1990). Scale-space and edge detection using anisotropic diffusion. *IEEE Transactions on pattern analysis and machine intelligence*, **12**(7), 629–639. <https://doi.org/10.1109/34.56205>
10. Gupta, D. (2023). Image segmentation keras: Implementation of segnet, fcn, unet, pspnet and other models in keras. *arXiv preprint arXiv:2307.13215*.
11. Li, K., Wang, Y., Zhang, J., Gao, P., Song, G., Liu, Y., Li, H., & Qiao, Y. (2023). Uniformer: Unifying convolution and self-attention for visual recognition. *IEEE Transactions on Pattern Analysis and Machine Intelligence*, **45**(10), 12581–12600.
12. Patro, B. N., Nambodiri, V. P., & Agneeswaran, V. S. (2023). SpectFormer: Frequency and Attention is what you need in a Vision Transformer. *arXiv preprint arXiv:2304.06446*. <https://doi.org/10.48550/arXiv.2304.06446>
13. Wang, W., Xie, E., Li, X., Fan, D.-P., Song, K., Liang, D., Lu, T., Luo, P., & Shao, L. (2021). Pyramid vision transformer: A versatile backbone for dense prediction without convolutions. *Proceedings of the IEEE/CVF international conference on computer vision*, Montreal, QC, Canada.
14. Han, D., Pan, X., Han, Y., Song, S., & Huang, G. (2023). Flatten transformer: Vision transformer using focused linear attention. *Proceedings of the IEEE/CVF International Conference on Computer Vision*, Paris, France.
15. Tu, Z., Talebi, H., Zhang, H., Yang, F., Milanfar, P., Bovik, A., & Li, Y. (2022). Maxvit: Multi-axis vision transformer. *European conference on computer vision*, Tel Aviv, Israel.
16. He, K., Zhang, X., Ren, S., & Sun, J. (2016). Deep residual learning for image recognition. *Proceedings of the IEEE conference on computer vision and pattern recognition*, Las Vegas, NV, USA.

17. Zhu, L., Liao, B., Zhang, Q., Wang, X., Liu, W., & Wang, X. (2024). Vision Mamba: Efficient Visual Representation Learning with Bidirectional State Space Model. *arXiv preprint arXiv:2401.09417*. <https://doi.org/10.48550/arXiv.2401.09417>
18. Reddy, C. D., Lopez, L., Ouyang, D., Zou, J. Y., & He, B. (2023). Video-Based Deep Learning for Automated Assessment of Left Ventricular Ejection Fraction in Pediatric Patients. *Journal of the American Society of Echocardiography*, **36**(5), 482–489. <https://doi.org/10.1016/j.echo.2023.01.015>